

Luminescent Metal–Organic Frameworks (MOFs) as a Chemopalette: Tuning the Thermo-chromic Behavior of Dual-Emissive Phosphorescence by Adjusting the Supramolecular Microenvironments

Shun-Ze Zhan,^[a] Mian Li,^[a] Seik Weng Ng,^[b, c] and Dan Li*^[a]

Abstract: Two classical copper(I)-cluster-based luminophores, namely, Cu_4I_4 and $[\text{Cu}_3\text{Pz}_3]_2$ (Pz = pyrazolate), are immobilized in a supramolecular system through the formation of metal–organic framework (MOF) materials. This series of luminescent MOF materials, namely, $[\text{Cu}_4\text{I}_4(\text{NH}_3)\text{Cu}_3(\mathbf{L1})_3]_n$, $[\text{Cu}_4\text{I}_4(\text{NH}_2\text{CH}_3)\text{Cu}_3(\mathbf{L1})_3]_n$, and $[\text{Cu}_4\text{I}_4\text{Cu}_3(\mathbf{L2})_3]_n$ ($\mathbf{L1}$ = 3-(4-pyridyl)-5-(*p*-tolyl)pyrazolate; $\mathbf{L2}$ = 3-(4-pyridyl)-5-(2,4-

dimethylphenyl)pyrazolate), exhibit diverse thermo-chromism attributed to the relative functioning efficacy of the two coordination luminophores. Such an intriguing chemopalette effect is

Keywords: copper • luminescence • metal–organic frameworks • supramolecular chemistry • thermo-chromism

regulated by the different supramolecular microenvironments between the two-dimensional layers of these MOFs, and in particular, by the fine-tuned Cu–Cu distances in the excimeric $[\text{Cu}_3\text{Pz}_3]_2$ luminophore. The structure–property elucidation of the thermo-chromic behavior allows one to understand these optical materials with unusual dual-emissive properties.

Introduction

The borders of chemical and material sciences have been vastly expanded since the introduction of the concept of supramolecular chemistry that brought a continual increase in interest in “the chemistry beyond the molecule”.^[1,2] Yet this classical definition of supramolecular chemistry, which specifies “the association of two or more chemical species held together by intermolecular forces”, triggered a controversy about whether some certain multicomponent systems, in which the components are linked by chemical bonds of various natures, can be considered supramolecular systems, especially in the field of supramolecular photochemistry.^[3–6] Thus, from a functional viewpoint, the operational definition of supramolecular species assesses the degree of intercomponent electron and/or energy transfer when stimulated by electron or photon inputs.^[4a]

Along with the increasing complexity of the focusing entities (from molecules to molecular assemblies or multicomponent systems) in supramolecular photochemistry, the burgeoning, and already fruitful, field of luminescent metal–organic framework (MOF) materials^[7] provides a new platform for the design and construction of supramolecular systems that are capable of performing light-induced functions, such as chemical sensors, light-emitting devices, and optical biomedicines.^[7b] These multicomponent photofunctional materials are usually highly crystalline supramolecular solids that consist of strong bonding, thereby enabling structural predictability and robustness, and organic linkages available for synthetic modification.^[7a] Given the various origins of MOF luminescence (mostly ligand-based, lanthanide-based, charge-transfer, and guest-induced luminescence),^[7] it is possible to achieve dual emissions^[8] by simultaneously incorporating diverse luminophores into one matrix by means of supramolecular interactions. This is an advantage relative to those of molecule-based dual emissions,^[8a–d] which are usually bounded by Kasha’s rule^[9] that permits only the lowest excited state to emit.

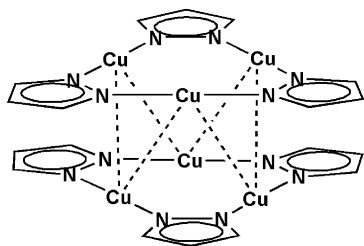
In our previous work,^[10] a supramolecular dual-emissive MOF, namely, $[\text{Cu}_4\text{I}_4(\text{NH}_3)\text{Cu}_3(\mathbf{L1})_3]_n$ (hereafter denoted as $\mathbf{1}\cdot\text{NH}_3$, $\mathbf{L1}$ = 3-(4-pyridyl)-5-(*p*-tolyl)pyrazolate), which contains two classical copper(I)-cluster-based luminophores, Cu_4I_4 and $[\text{Cu}_3\text{Pz}_3]_2$ (Scheme 1; Pz = pyrazolate), was reported. The tetrahedral Cu_4I_4 cluster is the most documented member in the copper(I) halide family,^[11] but it is still of considerable research interest because of its structural applicability to act as the secondary building unit of MOFs,^[12] and its well-studied, yet still developing, photophysical functionality.^[13] Compared with the luminescence origin of Cu_4I_4 that is a triplet cluster-centered excited state (^3CC , coupled

[a] Dr. S.-Z. Zhan, M. Li, Prof. Dr. D. Li
Department of Chemistry and Research Institute
for Biomedical and Advanced Materials
Shantou University, Guangdong 515063 (P.R. China)
Fax: (+86) 754-82902767
E-mail: dli@stu.edu.cn

[b] Prof. Dr. S. W. Ng
Department of Chemistry, University of Malaya
50603 Kuala Lumpur (Malaysia)

[c] Prof. Dr. S. W. Ng
Chemistry Department, Faculty of Science
King Abdulaziz University
P.O. Box 80203 Jeddah (Saudi Arabia)

Supporting information for this article is available on the WWW under <http://dx.doi.org/10.1002/chem.201204632>.



Scheme 1. Dimer of trimers of the $[\text{Cu}_3\text{Pz}_3]_2$ cluster with energetically favored staggered stacking mode,^[14b,15c] in which the ligand-unsupported intertrimeric Cu–Cu contacts are highlighted by dashed lines.

with halide-to-ligand charge-transfer excited state, ³XLCT,^[13a,b] the bright phosphorescence of the $[\text{Cu}_3\text{Pz}_3]_2$ cluster (Scheme 1) is attributed to the excimer formation of the dimer of trimers.^[14] This excimer regulated by means of intertrimeric Cu–Cu contacts (which vary from approximately 2.9 to 4.6 Å^[15a,e]) are subject to the influences of substituent effects^[15c] and supramolecular microenvironments (e.g., stacking effects in the crystalline state) in both discrete^[15] and polymeric^[10,16] forms, thus triggering several interesting photophysical types of behavior, especially luminescence thermochromism.^[10,15b]

A merit of this supramolecular system that incorporates both Cu_4I_4 and $[\text{Cu}_3\text{Pz}_3]_2$ is their well-resolved emissions that can be excited under different wavelengths (Cu_4I_4 : $\lambda_{\text{ex}} = 350\text{--}400$, $\lambda_{\text{em}} = 540\text{--}580$ nm; $[\text{Cu}_3\text{Pz}_3]_2$: $\lambda_{\text{ex}} = 270\text{--}320$, $\lambda_{\text{em}} = 630\text{--}720$ nm).^[10] This provides the possibility that $\mathbf{1}\cdot\text{NH}_3$ can be populated to its two stable excited states under different irradiations, and then give two distinguishable emission maxima (i.e., dual emissions) through electron/energy transfer in the thermal equilibrium process. In an attempt to acquire more sophisticated manipulation of the luminescent and thermochromic behaviors, one can consider tuning the relative functioning efficacy of the two coordination luminophores, which can contribute cooperatively to the visual color of the phosphorescent MOF material. This strategy is termed the “chemopalette” effect, and it can be achieved by means of adjusting the supramolecular microenvironment while maintaining the overall host framework (by taking advantage of the predictable structures of MOFs^[7b]).

In this regard, relative to the configurationally more rigid Cu_4I_4 cluster, the ligand-unsupported excimeric $[\text{Cu}_3\text{Pz}_3]_2$ cluster (Scheme 1) is more sensitive (reflected by its various packing modes and varying Cu–Cu distances^[15e]) to the variation in the supramolecular microenvironment that involves host–host and host–guest interactions, and crystal-stacking effects.^[15,16] Interestingly, $\mathbf{1}\cdot\text{NH}_3$ exhibits a double-layer stacking pattern,^[10] in which every two adjacent layers are connected by multiple interlayer Cu–Cu interactions in the $[\text{Cu}_3\text{Pz}_3]_2$ cluster. Herein, the “chemopalette” strategy is realized by modifying two chemically inactive sites (see below) in the host framework to adjust the supramolecular microenvironment, and to fine-tune the interlayer Cu–Cu distances in the $[\text{Cu}_3\text{Pz}_3]_2$ luminophore, thus manipulating the thermochromic behavior of the dual emissive MOF materials.

Experimental Section

Materials and physical measurements: Commercially available chemicals were used without further purification. Infrared spectra were obtained in KBr disks using a Nicolet Avatar 360 FTIR spectrometer in the range of 4000–400 cm^{-1} . ¹H NMR spectroscopy was performed using a Bruker DPX 400 spectrometer with tetramethylsilane as internal standard. All δ values are given in ppm. Elemental analyses of C, H, and N were determined using an Elementar Vario EL cube CHNS analyzer. Thermogravimetric (TG) analyses were performed using a TA Instruments Q50 thermogravimetric analyzer under nitrogen flow (40 mL min^{-1}) at a typical heating rate of 10 $^\circ\text{C min}^{-1}$. X-ray powder diffraction (XRPD) experiments were performed using a D8 Advance X-ray diffractometer.

Steady-state photoluminescence spectra and lifetime measurements were measured by a single-photon counting spectrometer using an Edinburgh FLS920 spectrometer equipped with a continuous Xe900 xenon lamp, a μF900 microsecond flash lamp, a red-sensitive Peltier-cooled Hamamatsu R928P photomultiplier tube (PMT), and a closed cycle cryostat (Advanced Research Systems). The corrections of excitation and emission for the detector response were performed ranging from 200 to 900 nm. The data were analyzed by iterative convolution of the luminescence decay profile with the instrument response function using the software package provided by Edinburgh Instruments. Lifetime data were fitted with triple-exponential-decay functions. The goodness of the nonlinear least-squares fit was judged by the reduced χ^2 value (< 1.3 in most of the cases), the randomness of the residuals, and the autocorrelation function (Table S4 and Figures S14–S16 in the Supporting Information). In all cases, the crystalline samples were selected under microscope with 40 \times amplification after being washed by ethanol and acetonitrile and then dried. The purity of the samples was assured by elemental analysis and X-ray powder diffraction measurement (Figure S19 in the Supporting Information).

Synthesis: Two ligands, 3-(4-pyridyl)-5-*p*-tolyl-1*H*-pyrazole (**HL1**) and 3-(4-pyridyl)-5-(2,4-dimethylphenyl)-1*H*-pyrazole (**HL2**), were used in this work. **HL1** was reported in our previous work,^[10] and **HL2** was prepared by using a similar procedure as described previously by our group with modifications.^[16f,17]

1-(4-Pyridyl)-3-(2,4-dimethylphenyl)-1,3-propanedione: Methyl isonicotinate (3.5 mL, 3.5 g, 0.025 mol) was added to a suspension of newly prepared $\text{C}_2\text{H}_5\text{ONa}$ (3.4 g, 0.05 mol) in anhydrous THF (100 mL). The mixture was stirred at room temperature for 10 min and then 2,4-dimethylacetophenone (3.7 mL, 3.7 g, 0.025 mol) was slowly added to the mixture. After completing the addition, the mixture was kept with stirring for about 10 h while equipped with a drying tube. Then the solvent was evaporated completely under reduced pressure. The residual was dissolved in diluted acetic acid solution (100 mL, 3 mol L^{-1}), left in a refrigerator at 0–4 $^\circ\text{C}$ for about 5 h, then filtered. Yellow solids were obtained and dried under vacuum to give the product (3.50 g, 55.3%). M.p. 122–125 $^\circ\text{C}$; ¹H NMR (400 MHz, CDCl_3 , 298 K): $\delta = 8.78$ (dd, $J = 4.5, 1.7$ Hz, 2H; CHpy), 7.74 (dd, $J = 4.5, 1.7$ Hz, 2H; CHpy), 7.55 (d, $J = 11.6$ Hz, 1H; CHph), 7.17–7.01 (m, 2H; CHph), 6.60 (s, 1H; CHC=CH), 2.55 (s, 3H; CH₃), 2.38 ppm (s, 3H; CH₃) (see Figure S1 in the Supporting Information).

Ligand HL2: 1-(4-Pyridyl)-3-(2,4-dimethylphenyl)-1,3-propanedione (2.53 g, 0.01 mol) was added to ethanol (50 mL). Then the mixture was treated with an excess amount of hydrazine (80%, 3 mL) and heated to reflux for 10 h. The solution was kept standing in air to allow the ethanol solvent to evaporate. After several days, nearly colorless crystalline solids were obtained and dried under vacuum (1.62 g, 65.0%). M.p. 206–208 $^\circ\text{C}$; ¹H NMR (400 MHz, CD_3OD): $\delta = 8.54$ (d, $J = 5.3$ Hz, 2H; CHpy), 7.88 (t, $J = 5.4$ Hz, 2H; CHpy), 7.32 (d, $J = 7.7$ Hz, 1H; CHph), 7.16 (s, 1H; CHph), 7.10 (d, $J = 7.7$ Hz, 1H; CHph), 6.91 (s, 1H; CHpz), 2.39 (s, 3H; CH₃), 2.35 ppm (s, 3H; CH₃) (see Figure S2 in the Supporting Information; see also Figures S3–S5 in the Supporting Information for the crystal structure descriptions of **HL2**); IR (KBr): $\tilde{\nu} = 3405$ (w), 3193 (m), 3139 (m), 3123 (m), 2982 (m), 2911 (m), 1605 (vs), 1557 (m), 1494 (s), 1428 (vs), 1216 (s), 1130 (m), 1083 (m), 966 (vs), 836 (s), 817 (vs), 788 (s), 697 (vs), 570 (s), 532 cm^{-1} (s).

Complexes: Compound **1**-NH₃ was reported in our previous work.^[10]

[Cu₄I₄(NH₂CH₃)Cu₃(L1)₃]_n (1**-NH₂CH₃):** A mixture of **HL1** (11.8 mg, 0.05 mmol), CuI (19.1 mg, 0.1 mmol), C₂H₅OH (3 mL), and one drop of aqueous methylamine (40%, about 0.05 mL) was sealed in an 8 mL hard glass tube and heated in an oven at 180 °C for 72 h, then slowly cooled to room temperature at a rate of 5 °C h⁻¹. Light yellow block crystals were obtained (25% yield based on the ligand). IR (KBr): $\tilde{\nu}$ = 3451 (w), 3368 (w), 3117 (w), 3054 (w), 3019 (w), 2911 (w), 2852 (w), 1612 (vs), 1475 (vs), 1421 (s), 1219 (m), 1111 (s), 1004 (m), 833 (m), 792 (m), 716 (m), 558 cm⁻¹ (m); elemental analysis calcd (%) for C₄₅H₃₉Cu₇I₄N₁₀: C 32.76, H 2.45, N 8.31; found: C 32.72, H 2.50, N 8.40.

[Cu₄I₄Cu₃(L2)₃]_n (2**):** A mixture of **HL2** (12.4 mg, 0.05 mmol), CuI (19.1 mg, 0.1 mmol), C₂H₅OH (3 mL), and one drop of aqueous ammonia (about 0.05 mL) was sealed in a 8 mL hard glass tube and heated in an oven at 180 °C for 72 h, then slowly cooled to room temperature at a rate of 5 °C h⁻¹. Light yellow block crystals were obtained (45% yield based on the ligand). IR (KBr): $\tilde{\nu}$ = 3120 (w), 3050 (w), 3006 (w), 2965 (w), 2943 (w), 1608 (vs), 1472 (vs), 1425 (s), 1219 (s), 1130 (m), 1004 (m), 830 (m), 795 (m), 713 (m), 532 cm⁻¹ (m); elemental analysis calcd (%) for C₄₈H₄₅Cu₇I₄N₁₀: C 33.97, H 2.49, N 7.43; found: C 34.05, H 2.51, N 7.51.

Crystal structure determination: Single-crystal data collections were performed using an Oxford Diffraction Gemini E (Enhance Mo_{K α} X-ray source, λ = 0.71073 Å) equipped with a graphite monochromator and an ATLAS CCD detector (CrysAlis CCD, Oxford Diffraction Ltd) under a cold nitrogen stream (100 K). The crystal structure data of **HL2** was collected at room temperature (293 K). The data were processed using CrysAlis RED, Oxford Diffraction Ltd (Version 1.171.34.44, release 25-10-2010 CrysAlis171.NET). Structures were solved by using direct methods (SHELXTL-97) and refined on F^2 using full-matrix least-squares cycles (SHELXTL-97).^[18] All non-hydrogen atoms were refined with anisotropic thermal parameters, and all hydrogen atoms were included in calculated positions and refined with isotropic thermal parameters riding on those of the parent atoms. Structural diagrams were produced by using the OLEX computer program.^[19] The vacant volumes within the crystal cells were calculated by using the PLATON computer program.^[20] Crystal data and structure refinement parameters are summarized in Table 1. Some key bond lengths and angles are given in Table 2.

CCDC-914928, 914929, and 914930 contain the supplementary crystallographic data for this paper. These data can be obtained free of charge from The Cambridge Crystallographic Data Centre via www.ccdc.cam.ac.uk/data_request/cif.

Results and Discussion

Realization of the chemopalette strategy: As stated above, the chemopalette strategy can be realized through fine-tuning the intertrimeric Cu–Cu distances in the [Cu₃Pz₃]₂ lu-

Table 1. Comparisons of some key bond lengths [Å], bond angles [°], and dihedral angles (χ in °) for the [Cu₃Pz₃]₂ unit of complexes **1**-NH₃, **1**-NH₂CH₃, and **2** in 100 K.

	1 -NH ₃ ^[10]	1 -NH ₂ CH ₃	2
bond lengths [Å]	N1–Cu1 1.869(2) N2–Cu1B 1.870(1)	Cu1–N1 1.860(3) Cu1–N8 1.865(4) Cu2–N4 1.867(4) Cu2–N2 1.875(4) Cu3–N7 1.863(3) Cu3–N5 1.867(4)	N1–Cu1 1.852(5) N2–Cu1A 1.865(5)
bond angles [°]	N1–Cu1–N2A 170.34(1)	N1–Cu1–N8 172.09(17) N4–Cu2–N2 169.99(16) N7–Cu3–N5 173.73(17)	N1–Cu1–N2B 171.80(3)
intratrimeric distances [Å]	Cu1–Cu1A 3.2240(6)	Cu1–Cu2 3.2090(7) Cu2–Cu3 3.2502(3)	Cu1–Cu1C 3.1727(2)
intertrimeric distances [Å]	Cu1–Cu1C 3.5953(7) Q1–Q1A ^[a] 3.075(8)	Cu1–Cu2A 3.4228(5) Cu1–Cu3A 3.8275(6) Cu2–Cu3A 3.7188(6) Q1–Q1A ^[a] 3.1579	Cu1–Cu1 3.6998(7) Q1–Q1C 3.214(5)
P _{Cu} χ P _{Pz}	19.9	22.5, 19.3, 15.4	16.1
P _{Phen} χ P _{Pz}	41.0	37.3, 35.3, 51.6	52.8
		symmetry codes	
A	–y+1, +x–y+1, +z	–x, –y, –z	–x+y, –x+1, +z
B	–x+y, –x+1, +z		–y+1, +x–y+1, +z
C	+y, –x+y+1, –z		+y–1/3, –x+y+1/3, –z+1/3

[a] Q: the center of the Cu₃ triangle in the Cu₃Pz₃ unit.

Table 2. Crystal data and structure refinement parameters for the ligand **HL2** and complexes **1**-NH₂CH₃ and **2**.

	HL2	1 -NH ₂ CH ₃	2
formula	C ₁₆ H ₁₅ N ₃	C ₄₆ H ₄₁ N ₁₀ Cu ₇ I ₄	C ₄₈ H ₄₂ N ₉ Cu ₇ I ₄
<i>M_r</i>	249.31	1681.48	1697.29
crystal system	monoclinic	triclinic	trigonal
space group	<i>P</i> 2 ₁ / <i>c</i>	<i>P</i> $\bar{1}$	<i>R</i> $\bar{3}$
<i>T</i> [K]	293(2)	100(2)	100(2)
<i>a</i> [Å]	6.8837(14)	13.4501(3)	18.5683(3)
<i>b</i> [Å]	22.420(6)	13.7366(2)	18.5683(3)
<i>c</i> [Å]	17.414(3)	13.8529(3)	28.7951(8)
α [°]	90	82.753(2)	90
β [°]	93.824(16)	85.525(2)	120
γ [°]	90	86.069(2)	90
<i>V</i> [Å ³]	2681.6(10)	2526.79(9)	8597.9(3)
<i>Z</i>	8	2	6
ρ_{calcd} [g cm ⁻³]	1.235	2.216	1.967
μ [mm ⁻¹]	0.0750	5.377	4.741
reflns collected	10750	36562	6367
unique reflns	4675	8880	3363
<i>R</i> _{int}	0.0450	0.0503	0.0221
GOF	1.110	1.062	1.065
<i>R</i> ₁ ^[a] (<i>I</i> > 2 σ (<i>I</i>))	0.0558	0.0312	0.0460
<i>wR</i> ₂ ^[b] (<i>I</i> > 2 σ (<i>I</i>))	0.1676	0.0519	0.1292
<i>R</i> ₁ ^[a] (all reflns)	0.0846	0.0429	0.0629
<i>wR</i> ₂ ^[b] (all reflns)	0.2178	0.0572	0.1433

[a] $R_1 = \Sigma(|F_o| - |F_c|) / \Sigma |F_o|$. [b] $wR_2 = [\Sigma w(F_o^2 - F_c^2)^2 / \Sigma w(F_c^2)^2]^{1/2}$.

minophore to regulate its functioning efficacy. In previous reports, several examples to adjust intertrimeric Cu–Cu contacts were documented, including physical manipulation (temperature^[15b,c,21a] or pressure^[21b]) and/or chemical manipulation (host–host^[16b–d] or host–guest^[22] interactions). In this work, a different chemical-manipulation approach that considers the crystal-stacking effects is utilized. As known,^[7b] MOFs structures are, to some extent, predictable and availa-

ble for pre- or post-synthetic modifications. The extended structure of $\mathbf{1}\cdot\text{NH}_3$ is a two-dimensional layer,^[10] and thus the interlayer supramolecular microenvironment and the overall crystal-stacking pattern can be easily influenced by the chemically inactive sites (steric effects) in the MOF structure. As shown in Figure 1a, two chemically inactive sites (I and II) in $\mathbf{1}\cdot\text{NH}_3$ are pre-synthetically modified through ligand replacement (site I) and decoration (site II).

In site I, the replacement of NH_3 with NH_2CH_3 , though subtle, would lead to the $\text{Cu}_4\text{I}_4\text{L}_4$ (L =three pyridyl and one NH_2CH_3) cluster losing the C_{3v} point symmetry, thus lowering the overall crystal symmetry. As a result, $\mathbf{1}\cdot\text{NH}_2\text{CH}_3$ crystallized in the triclinic $P\bar{1}$ space group (Table 1) relative to the trigonal $R\bar{3}$ of $\mathbf{1}\cdot\text{NH}_3$. In site II, the additional decoration of a *meta*-methyl (from 4-methylphenyl in **HL1** to 2,4-dimethylphenyl in **HL2**; Figure S2–S5 in the Supporting Information) would increase the steric hindrance, thus influencing the interlayer stacking pattern. Such steric effects are evidenced by the larger dihedral angles between the pyra-

zole ring and phenyl ring (52.16 and 49.22°) than those between pyrazole ring and pyridyl ring (7.02 and 15.56°) in the crystal structure of **HL2** (Figure S3 in the Supporting Information). Although **2** also crystallized in trigonal $R\bar{3}$ space group, the stacking mode is significantly different from those of $\mathbf{1}\cdot\text{NH}_3$ and $\mathbf{1}\cdot\text{NH}_2\text{CH}_3$ (see below).

It is notable that one Cu site in the Cu_4I_4 unit of **2** is three-coordinated, unlike the situations in $\mathbf{1}\cdot\text{NH}_3$ and $\mathbf{1}\cdot\text{NH}_2\text{CH}_3$. This is reflected by the small residual peak (less than 1.0) around the vacant Cu site in the crystal refinement of **2**, and further supported by IR and elemental analyses. Similar synthetic procedures that involve **HL2** and aqueous methylamine or ethylamine resulted in the same product, **2**. Such an unusual coordination mode in Cu_4I_4 -related complexes has been rarely reported,^[12c,g] but can be observed in our other unpublished works.

Adjustments of supramolecular microenvironments: There are two sets of notable variations in the microenvironments

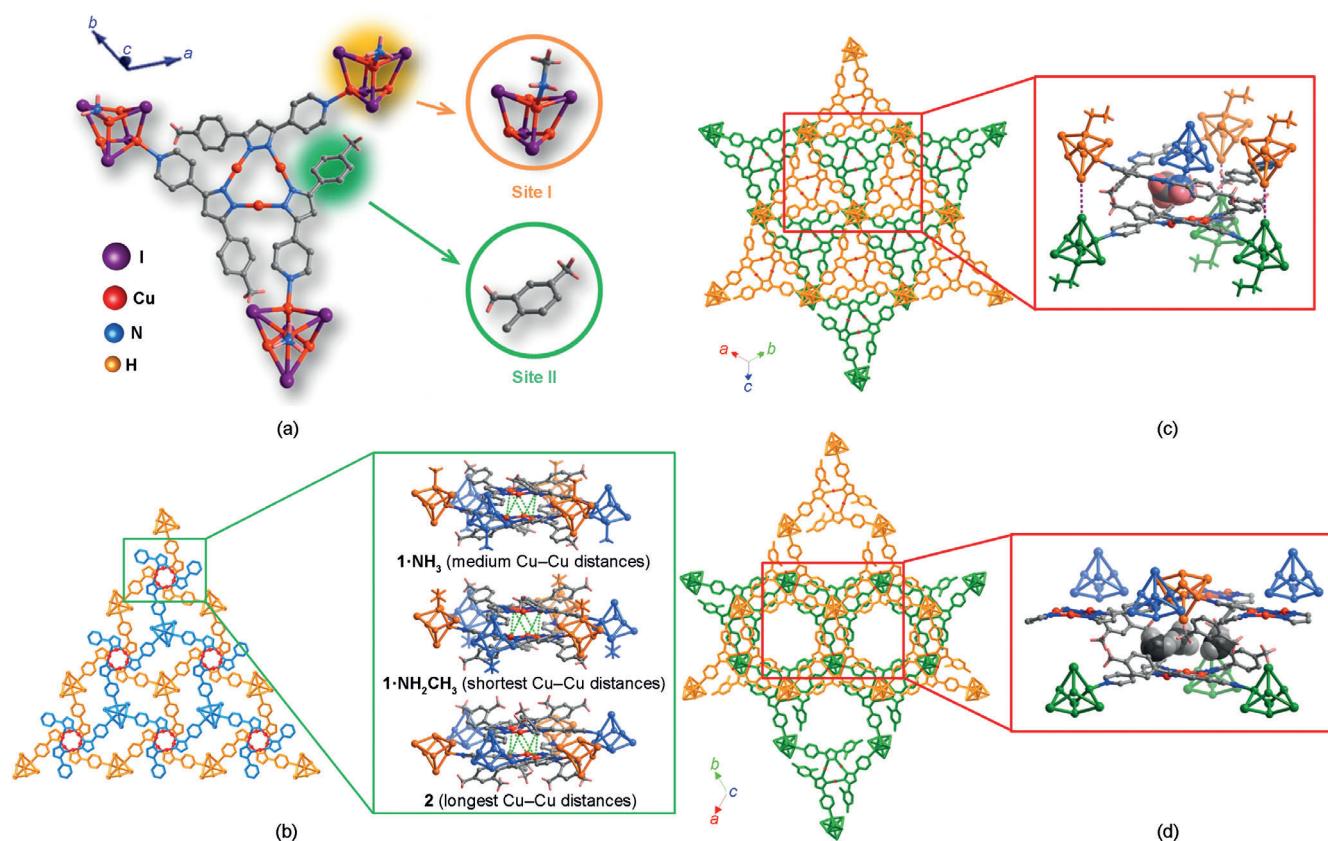


Figure 1. a) Schematic representation of the chemopalette strategy in the supramolecular system of $\mathbf{1}\cdot\text{NH}_3$ and b–d) the supramolecular microenvironments of Cu_3Pz_3 and Cu_4I_4 coordination luminophores. a) Illustration of the two inactive sites (site I and site II) modified in $\mathbf{1}\cdot\text{NH}_2\text{CH}_3$ and **2** to adjust the supramolecular microenvironments. Hydrogen atoms in pyrazolate and phenyl rings are omitted. b) Representation of the supramolecular microenvironments within the double-layer motif. Left: Top view showing the similarity of the double-layer (blue and orange) stacking patterns of the three MOFs. Right: Partial side views showing the subtle distinctions of the microenvironments within and around the $[\text{Cu}_3\text{Pz}_3]_2$ clusters in $\mathbf{1}\cdot\text{NH}_3$, $\mathbf{1}\cdot\text{NH}_2\text{CH}_3$, and **2**, respectively. Cu–Cu contacts in green dashed lines within $[\text{Cu}_3\text{Pz}_3]_2$; the surrounding Cu_4I_4 clusters from different layers are shown in blue and orange as in the top view. c, d) Representation of the supramolecular microenvironments between two double-layer motifs (note that the orange layers remain in the same position). Left: Top views showing the different outer-double-layer (orange and green) stacking patterns of c) $\mathbf{1}\cdot\text{NH}_2\text{CH}_3$ and d) **2**. Right: Partial side views showing the distinctions of the steric effects and supramolecular interactions in c) $\mathbf{1}\cdot\text{NH}_2\text{CH}_3$ and d) **2**. Cu_4I_4 clusters from different layers are shown in orange and green as in the top view, and Cu_4I_4 clusters from another layer within the double-layer motif are shown in blue (as in b). The c) methylamine and d) *meta*-methyl groups that show steric effects are shown in the space-filling mode, and possible c) I–I contacts are shown in purple dashed lines.

in this supramolecular system. The first set concerns the $[\text{Cu}_3\text{Pz}_3]_2$ clusters that involve Cu–Cu contacts that link two adjacent layers to form a double-layer motif (Figure 1b). If one omits the two chemically inactive sites (I and II), the stacking patterns of the double-layer motif are similar in all three structures (Figure 1b, left; see Ref. [10] for the detailed structural description of $\mathbf{1}\cdot\text{NH}_3$).

The major distinctions are made by analyzing the interlayer Cu–Cu distances (at 100 K; see Figure 1b right and Table 1). For $\mathbf{1}\cdot\text{NH}_2\text{CH}_3$, the lower symmetry (triclinic $P\bar{1}$ versus trigonal $R\bar{3}$ of $\mathbf{1}\cdot\text{NH}_3$) is responsible for the distorted configuration of the $[\text{Cu}_3\text{Pz}_3]_2$ core, which exhibits three types of intertrimeric Cu–Cu distances, with the shortest one

being 3.422(8) Å (shorter than 3.595(2) Å in $\mathbf{1}\cdot\text{NH}_3$). These values are even shorter than those (3.628 Å) of the optimized geometry of the staggered mode of $[\text{Cu}_3\text{Pz}_3]_2$ in the ground state.^[14b] For $\mathbf{2}$, the steric effects of the dimethyl substituent lead to a longer intertrimeric Cu–Cu distance of 3.699(7) Å. This steric hindrance is also reflected in the dihedral angles between the phenyl and pyrazolate planes ($\mathbf{1}\cdot\text{NH}_3$: 41.0°; $\mathbf{1}\cdot\text{NH}_2\text{CH}_3$: 37.3, 35.3, and 51.6°; $\mathbf{2}$: 52.8°), with $\mathbf{2}$ being the largest. The planarity of the Cu_3Pz_3 trimers, reflected in the dihedral angles between the Cu_3 and pyrazolate planes ($\mathbf{1}\cdot\text{NH}_3$: 19.9°; $\mathbf{1}\cdot\text{NH}_2\text{CH}_3$: 22.5, 19.3, and 15.4°; $\mathbf{2}$: 16.1°), consists of intertrimeric Cu–Cu distances, with the smallest dihedral angle corresponding to the longest intertrimeric Cu–Cu distances in $\mathbf{2}$. These data are shown in Table 1. This is consistent with the finding that shorter Cu–Cu distances (and hence stronger Cu–Cu contacts) would affect and reduce the Cu_3Pz_3 ring planarity.^[14a, 15c]

The second set of variations results in the relative sliding between two double-layer motifs (Figure 1c,d, and Figures S6 and S7 in the Supporting Information), which also contributes to the overall crystal-stacking effects in the three MOFs. The outer double-layer stacking pattern of $\mathbf{1}\cdot\text{NH}_2\text{CH}_3$ is similar to that of $\mathbf{1}\cdot\text{NH}_3$, which shows a packing arrangement of Cu_4I_4 – Cu_4I_4 , Cu_3Pz_3 –void, and void– Cu_3Pz_3 (the void represents the triangular space surrounded by three Cu_3Pz_3 units) along the [111] direction (Figure 1c, left). A detailed structural analysis reveals the steric effects and supramolecular interactions in this microenvironment (Figure 1c, right). Although not valid for a single contact (typical I⋯I interactions should range from 2.93 to 3.52 Å), the structure of $\mathbf{1}\cdot\text{NH}_2\text{CH}_3$ experiences cooperative, multiple I⋯I contacts (3.930 Å, compared with 3.879 Å in $\mathbf{1}\cdot\text{NH}_3$) in the Cu_4I_4 – Cu_4I_4 zones. The arrangement is also stabilized by sets of C–H⋯I contacts (C⋯I distances: 3.916–4.285 Å). Note that the void in the orange layer (Figure 1c, left) allows the Cu_4I_4 cluster with a methylamine hook from the upper blue layer to plug in and make contact with the Cu_3Pz_3 unit (N⋯Cu distances: 3.489, 3.852, and 3.982 Å, compared with 3.419 Å in $\mathbf{1}\cdot\text{NH}_3$) in the void– Cu_3Pz_3 zone (Figure 1c, right).

Unlike the case of $\mathbf{1}\cdot\text{NH}_2\text{CH}_3$, compound $\mathbf{2}$ exhibits an outer double-layer stacking pattern of Cu_4I_4 – Cu_3Pz_3 , Cu_3Pz_3 – Cu_4I_4 , and void–void along the *c* axis (Figure 1d, left). This packing pattern can be viewed as the relatively vertical sliding of the orange and green layers in the two complexes. A vital factor for this sliding is the steric hindrance of the *meta*-methyl decorations, which prevent the Cu_4I_4 cluster in the blue layer from approaching the Cu_3Pz_3 unit in the green layer (Figure 1d, right). This creates the void–void zones in the structure, and hence there is an approximately 415 Å³ (4.82%, calculated by PLATON) vacancy within one unit cell. For this reason, the crystal density of $\mathbf{2}$ (1.967 g cm^{−3}) is also smaller than those of $\mathbf{1}\cdot\text{NH}_3$ and $\mathbf{1}\cdot\text{NH}_2\text{CH}_3$ (2.225 and 2.216 g cm^{−3}, respectively). In the Cu_4I_4 – Cu_3Pz_3 and Cu_3Pz_3 – Cu_4I_4 zones, there exist sets of C–H⋯I contacts (C⋯I distances: 4.035–4.081 Å).

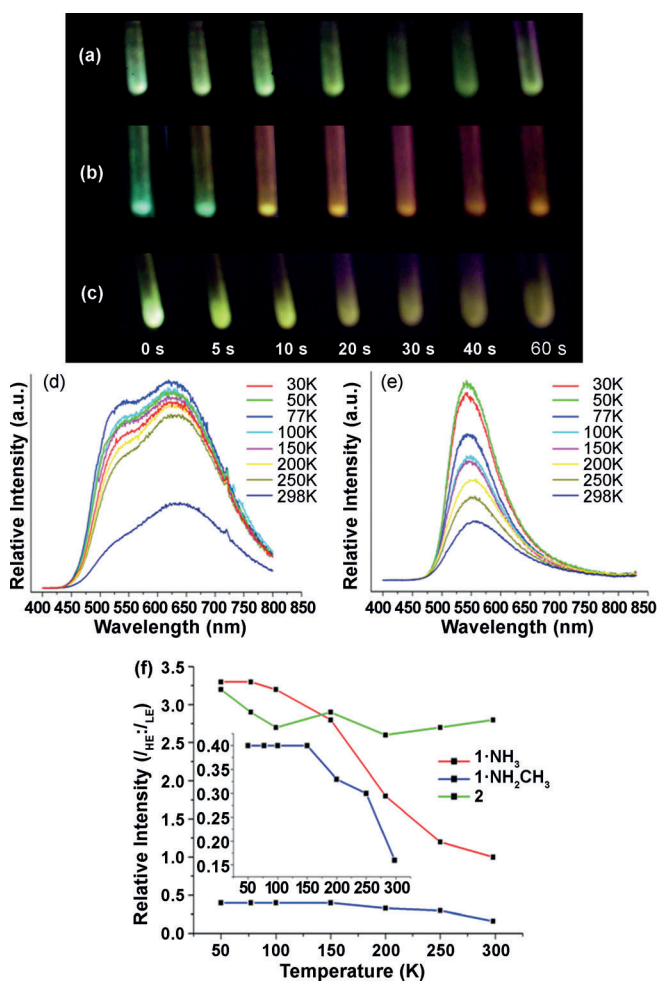


Figure 2. Photoluminescence images of the three complexes a) $\mathbf{1}\cdot\text{NH}_3$, b) $\mathbf{1}\cdot\text{NH}_2\text{CH}_3$, and c) $\mathbf{2}$ upon a treatment in a liquid nitrogen bath (77 K). The samples were packed in Suprasil quartz tubes and then immersed in the liquid nitrogen for a few minutes, after which the tubes were taken out to let them recover to room temperature in air; meanwhile, they were exposed to the irradiation of a UV lamp (365 nm) to observe the color changes within a period of 60 s. d, f) Temperature-dependent (30–298 K) solid-state luminescence spectra of d) $\mathbf{1}\cdot\text{NH}_2\text{CH}_3$ and e) $\mathbf{2}$ upon excitation at 370 nm, and f) plots showing the changing tendency of the relative intensity ($I_{\text{HE}}/I_{\text{LE}}$) of the two Gaussian peaks upon temperature variation. The inserted plot in (f) amplifies the vertical scale for the $I_{\text{HE}}/I_{\text{LE}}$ ratio of $\mathbf{1}\cdot\text{NH}_2\text{CH}_3$.

Thermochromic behaviors of luminescent MOFs: As communicated in our previous work,^[10] **1**·NH₃ exhibited interesting reversible luminescence thermochromism from green (77 K) to yellow (293 K). In the high-temperature range (293–413 K), the luminescence changed from bright yellow to dark orange-red upon heating, and this chromic process was also reversible upon cooling. It was suggested that such thermochromic behavior is the consequence of a thermal equilibrium that involves the energy transfer between two competitive excited states that originate from the Cu₄I₄ and [Cu₃Pz₃]₂ (more precisely, the triplet acceptor of the excimer) luminophores, respectively (see Figure S17 in the Supporting Information for proposed potential-energy diagram).^[10] This hypothesis is the foundation of the chemopalette strategy, for which the tunability of the visual luminescent color is attributed to the relative functioning efficacy of the Cu₄I₄ and [Cu₃Pz₃]₂ clusters in this supramolecular system. In this work, the subtle adjustments of the supramolecular microenvironments in **1**·NH₂CH₃ and **2**, especially for the fine-tuned Cu–Cu distances (Table 1), do affect the luminescence efficacy of [Cu₃Pz₃]₂ and the subsequent thermochromic behavior, thus again verifying the above hypothesis. As shown in Figure 2a–c, when treated with a liquid-nitrogen bath and exposed under UV lamp (365 nm), the thermochromic behaviors of the three luminescent MOFs are different. Under cryogenic conditions (77 K), all three MOFs show intense green luminescence. In contrast, when recovering to room temperature, the sample of **1**·NH₃ changes its emissive color from green to yellow with its brightness weakening; **1**·NH₂CH₃ undergoes more marked color changes from blue-green to yellow and then to dark orange; the sample of **2** experiences bright green-yellow to fading yellow within the 60 s period. These observations verify the effectiveness of the chemopalette strategy, which can be further supported by the emission and lifetime measurements.

Phosphorescence with tunable dual emissions: The luminescence spectra and lifetimes of **1**·NH₃ were reported elsewhere.^[10] Two emission bands with the peaks at approximately 540 (higher energy, or HE) and 680 nm (lower energy, or LE) occurred at room temperature (see Figure S8 in the Supporting Information for Gaussian fits), and the triplet-excited *Cu₄I₄ (*Cu₄) and triplet excimeric *[Cu₃Pz₃]₂ (*Cu₆) were responsible for the HE and LE emissions, respectively. The molar ratio of the two luminophores (*Cu₄·*Cu₆) is 2:1 in all three MOFs. The lower-energy excitation (370 nm) would first populate the *Cu₄ triplet state, followed by the subsequent energy transfer that could sensitize the [Cu₃Pz₃] trimer to its triplet excited state (triplet acceptor), and then the excimer formation of the dimer-of-trimers *Cu₆ triplet state through one excited trimer reacting with another ground-state trimer. In short, the [Cu₃Pz₃] triplet acceptor is involved in the energy-transfer process, whereas the *[Cu₃Pz₃]₂ excimer is responsible for the LE emission. Herein, the adjustments of the supramolecular microenvironments in **1**·NH₂CH₃ and **2** that lead to the subtle

variation in the Cu–Cu distances in [Cu₃Pz₃]₂ are supposed to affect the relative intensity of the LE bands in the emission spectra. The thermochromic behaviors are believed to involve a thermally activated energy transfer,^[10] but a more complex photophysical process that involves the generation of new excited states under cryogenic conditions is highly possible (see below).

According to the temperature-dependent emission spectra of **1**·NH₂CH₃ (Figure 2d), the LE bands with the peaks at approximately 630–650 nm are prevailing (compared with the HE bands that peaked at approximately 520–530 nm) over the whole temperature range, unlike the situation of **1**·NH₃ in which the HE bands dominate.^[10] This is consistent with the structural feature of the shortest intertrimeric Cu–Cu distances in **1**·NH₂CH₃ (Figure 1b and Table 1). The HE and LE bands are partly overlapped, which can be perfectly fitted to two Gaussian peaks, for example, at 298 K, with maxima at 524 nm ($\approx 19083\text{ cm}^{-1}$) and 641 nm ($\approx 15600\text{ cm}^{-1}$) and full width at half-maximum (fwhm) values of approximately 3477 cm^{-1} and approximately 2808 cm^{-1} , respectively ($R^2=0.9949$; $\chi^2=0.56\times 10^{-3}$; Figure S8 in the Supporting Information). The same procedure was applied to the emission spectra of **1**·NH₃, thus giving two peaks at 538 nm ($\approx 18587\text{ cm}^{-1}$) and 676 nm ($\approx 14793\text{ cm}^{-1}$) and fwhm values of approximately 4154 cm^{-1} and approximately 2765 cm^{-1} , respectively, at 298 K ($R^2=0.9879$; $\chi^2=1.02\times 10^{-3}$; Figure S9 in the Supporting Information).

Careful examination of the fitted Gaussian peaks at various temperatures reveals that the intensity of the two emission bands in **1**·NH₂CH₃ increased simultaneously upon cooling, consistent with the much brighter luminescence under lower temperature, which is probably due to the reduced nonradiative transition. However, the increment rates of the HE and LE bands are different. The relative intensity ratio ($I_{\text{HE}}:I_{\text{LE}}$) of **1**·NH₂CH₃ increases more than twice from 0.16 to 0.4 (Figure 2f and Table S3 in the Supporting Information), thus indicating a faster increment speed of the HE band upon cooling. Such different increment rates led to the emission color change from orange to green, which is responsible for the thermochromism. In comparison, for **1**·NH₃, the relative intensity of the LE band decreases drastically upon cooling, whereas the HE band intensity increases steadily, thereby giving rise to the changes of $I_{\text{HE}}/I_{\text{LE}}$ from 1.0 to 3.3 (Figure 2f and Table S3 in the Supporting Information).

Commonly, upon cooling, the emission intensity should increase due to reduced nonradiative transition. However, for **1**·NH₃, the unusual decrease in the LE band at lower temperatures can be assigned to the reduced efficiency of thermally activated energy transfer from the HE to LE bands,^[10] given that the lower-energy excitation (370 not 270 nm) does not match with the *Cu₆ LE band. In contrast, for **1**·NH₂CH₃, the HE-to-LE energy transfer seems efficient given the prevailing LE bands at all temperatures (Figure 2d) despite being excited at 370 nm. This should be related to the strongest intertrimeric Cu–Cu interactions in

$\mathbf{1}\cdot\text{NH}_2\text{CH}_3$, which would reduce the energy level of the $[\text{Cu}_3\text{Pz}_3]$ triplet acceptor (mediated by Cu–Cu contacts), and thus bring down the overall potential-energy curve for $^*\text{Cu}_6$ (Figure S17 in the Supporting Information)^[10] and its crossing point with the $^*\text{Cu}_4$ potential-energy curve. Accordingly, the energy barrier (ΔE_1 in Figure S17 in the Supporting Information)^[10] of the HE-to-LE transition can be reduced to populate a larger number of $[\text{Cu}_3\text{Pz}_3]$ triplet acceptor, thereby yielding more $^*\text{Cu}_6$ excimers. These results suggest that the populations of the $^*\text{Cu}_6$ excited states in $\mathbf{1}\cdot\text{NH}_2\text{CH}_3$ and $\mathbf{1}\cdot\text{NH}_3$ are not equal, and can be regulated by the fine-tuned Cu–Cu contacts that are extremely sensitive to distance variation. Note that for $\mathbf{1}\cdot\text{NH}_2\text{CH}_3$ the shortening of the Cu–Cu distance to 3.4228 Å (compared with the theoretically optimized value of 3.628 Å^[14b]) is considered significant because the Cu–Cu interaction dies off rapidly as a function of distance (approximately r^{-6} dependence^[14b]).

It is noteworthy that the crystal structures of the MOFs are measured at 100 K, and it would be expected that, for $\mathbf{1}\cdot\text{NH}_2\text{CH}_3$, the shortening of intertrimeric Cu–Cu distances in $\mathbf{1}\cdot\text{NH}_2\text{CH}_3$ will result in the redshift of the LE band at 100 K, in addition to the increase in intensity as discussed above. However, a slight blueshift (LE bands peak at 631 nm for $\mathbf{1}\cdot\text{NH}_2\text{CH}_3$ and 639 nm for $\mathbf{1}\cdot\text{NH}_3$, respectively; Figures S8 and S9 in the Supporting Information) is observed. This indicates that a more complex process is occurring, in which the electronic structure is modified by the change in temperature. If such an excited-state adjustment does not interrupt the energy-transfer process, one would expect an identical isoluminescent point^[23] (the counterpart of the isosbestic point^[23a] in absorption spectra) between the HE and LE bands. Yet the isoluminescent points in the emission spectra of $\mathbf{1}\cdot\text{NH}_3$ alter from 630 to 650 nm upon progressive cooling (Figure S11 in the Supporting Information). Such a shift means that a new excited species formed, further evidenced by the blueshift of the LE emission band and supported by the literature.^[21a] By carefully examining the emission spectra upon cooling, we found that the HE band remains almost unaltered, but the LE band shows an apparent blueshift from 676 nm at 298 K to 613 nm at 50 K (Figure S9 in the Supporting Information). Such a blueshift phenomenon in trinuclear pyrazolate systems was reported by Omary et al.^[21a] through combined experimental and computational research. They offered insights into the generality of this interesting counterintuitive spectral shift: It concerns the generation of multiple $^*[\text{Cu}_3\text{Pz}_3]_2$ excited states, rather than a mere blueshift of one band. The singlet-to-triplet intersystem crossing can give rise to multiple phosphorescent $^*[\text{Cu}_3\text{Pz}_3]_2$ states, and this relaxation might be hindered at low temperatures to populate higher-energy triplet states. The internal conversion between different triplet states is possible upon progressive heating, and thus luminescence thermochromism is observed. This rationale is valid for the LE band of this MOF system, and might be responsible for the isoluminescent point shift.

The photoluminescence decay profiles of $\mathbf{1}\cdot\text{NH}_2\text{CH}_3$ at all measured temperatures monitored by 530 (HE) and 630 nm

(LE) under excitation at 370 nm were fitted with triexponential curves, with the lifetimes of approximately 2, 5–10, and 10–15 μs (Figures S14 and S15, and Table S4 in the Supporting Information), consistent with the results and assignment of the lifetimes of $\mathbf{1}\cdot\text{NH}_3$.^[10] The microsecond-scale lifetimes indicate phosphorescence, and the slight increase in the lifetime values upon cooling is due to the reduction of the nonradiative decay rate.

For $\mathbf{2}$, the temperature-dependent emission spectra (Figure 2e) depict predominant HE bands with peaks at 556 nm at all temperatures, accompanied by broad tailings in the LE regions. The structural feature of the longest intertrimeric Cu–Cu distances in $\mathbf{2}$ (Figure 1b and Table 1) supports this luminescence profile. With temperature cooling, the intensity of the HE band increases gradually, thereby leading to the emission color changes. The Gaussian fitting applied to these spectral bands (Figure S10 in the Supporting Information) gives, for example, at 298 K, two Gaussian peaks at 556 (HE) and 646 nm (LE) with the $I_{\text{HE}}/I_{\text{LE}}$ ratio of 2.8 ($R^2=0.9899$; $\chi^2=1.04\times 10^{-3}$), which are ascribed to $^*\text{Cu}_4$ and $^*\text{Cu}_6$ luminophores, respectively. The relative intensity of the HE and LE bands under different temperatures does not vary remarkably (Figure 2f and Table S3 in the Supporting Information), thus indicating that the thermally activated energy transfer from the HE to LE bands in $\mathbf{2}$ is inefficient, probably due to the longer Cu–Cu distances (and hence weaker Cu–Cu contacts) that raise the energy level of the $[\text{Cu}_3\text{Pz}_3]_2$ cluster at both the ground and excited states, and that generate a higher barrier for energy transfer. The very weak intensity of the LE bands does not rule out the possibility of partial population of the $^*\text{Cu}_6$ state directly from the 370 nm irradiation. The photoluminescence decay profile of $\mathbf{2}$ (Figure S16 and Table S4 in the Supporting Information) is similar to those of $\mathbf{1}\cdot\text{NH}_2\text{CH}_3$ and $\mathbf{1}\cdot\text{NH}_3$, but it is noted that for $\mathbf{2}$ the fractional contribution of τ_3 is much smaller, sometimes even trivial by comparison, than the cases of $\mathbf{1}\cdot\text{NH}_2\text{CH}_3$ and $\mathbf{1}\cdot\text{NH}_3$. This is consistent with the assignment of τ_1 and τ_2 to $^*\text{Cu}_4$ and τ_3 to $^*\text{Cu}_6$.^[10]

The effect of the excitation wavelength in this system was also examined. According to the excitation spectra (Figure S12 in the Supporting Information), the emission bands of $\mathbf{1}\cdot\text{NH}_2\text{CH}_3$ and $\mathbf{2}$ excited at 270 nm under different temperatures are measured (Figure S20 in the Supporting Information). Relative to those excited at 370 nm (Figure S21 in the Supporting Information), it was found that the relative intensity of the HE and LE bands both decrease. Note that this is unusual for the LE emissions, given that the 270 nm excitation matches better with the $^*\text{Cu}_6$ excited state, but this is another piece of direct spectral evidence for the proposed HE-to-LE energy-transfer process in this supramolecular MOF system.

Another striking feature in the luminescence profile of this MOF system is the absence of the even-higher energy band (450–500 nm) that accounts for the $^3\text{XLCT}$ of Cu_4I_4 , which was commonly observed in those discrete Cu_4I_4 complexes, such as $\text{Cu}_4\text{I}_4\text{Py}_4$ ^[13a] and $\text{Cu}_4\text{I}_4(\text{PPh}_3)_4$.^[13c,d] But it is also noted that the $^3\text{XLCT}$ band has been reported rarely for

Cu₄I₄ cluster-based coordination polymers.^[11] This mystery deserves to be explored in future research efforts.

Conclusion

In this work, a chemopalette strategy based on a supramolecular luminescent MOF system that involves Cu₄I₄ and [Cu₃Pz₃]₂ luminophores has been developed. The three complexes discussed in this context, namely, **1**-NH₃, **1**-NH₂CH₃, and **2**, exhibit different interesting thermochromic behaviors regulated by the modification of two chemically inactive sites in the MOFs and the subsequent adjustments of the supramolecular microenvironments, particularly the fine-tuned Cu–Cu distances in [Cu₃Pz₃]₂. Several pieces of structural and spectral evidence point to the origin of an HE-to-LE energy-transfer process coupled with an internal conversion between multiple triplet states of the LE band. This electron/energy transfer is responsible for the MOF dual emissions and thermochromism.

Such an investigation sheds light on how one might apply the operational definition of supramolecular species to luminescent MOF materials, and is a good example of the elucidation of the structure–luminescence relationship in the MOF realm. The control of the thermochromic behavior enables one to understand these optical materials with unusual dual-emissive properties. This finding might find practical use for making thermometer-like phosphorescence-emitting devices. The chemopalette strategy^[24] will be utilized in our further work by considering not only the tunable functionality of [Cu₃Pz₃]₂, but also that of Cu₄I₄ and other effects.

Acknowledgements

This work was financially supported by the National Basic Research Program of China (973 Program, nos. 2012CB821706 and 2013CB834803), the National Natural Science Foundation for Distinguished Young Scholars of China (no. 20825102), and the National Natural Science Foundation of China (nos. 21171114 and 91222202). S.W.N thanks the support from the Ministry of Higher Education of Malaysia (no. UM.C/HIR-MOHE/SC/03).

- [1] J.-M. Lehn, *Supramolecular Chemistry: Concepts and Perspectives*, VCH, Weinheim, **2002**.
- [2] J. W. Steed, J. L. Atwood, *Supramolecular Chemistry*, 2nd ed., Wiley, New York, **2006**.
- [3] V. Balzani, A. Credi, M. Venturi, *Molecular Devices and Machine: Concepts and Perspectives for the Nanoworld*, Wiley-VCH, Weinheim, **2009**.
- [4] a) V. Balzani, G. Bergamini, S. Campagna, F. Puntoriero, *Top. Curr. Chem.* **2007**, *280*, 1; b) M. Venturi, E. Marchi, V. Balzani, *Top. Curr. Chem.* **2011**, *323*, 73.
- [5] a) N. Armaroli, G. Accorsi, F. Cardinali, A. Listorti, *Top. Curr. Chem.* **2007**, *280*, 69; b) A. Barbieri, G. Accorsi, N. Armaroli, *Chem. Commun.* **2008**, 2185.
- [6] a) *Photofunctional Transition Metal Complexes (Structure and Bonding)* (Ed.: V. W.-W. Yam), Springer, Berlin Heidelberg, **2007**; b) K. M.-C. Wong, V. W.-W. Yam, *Acc. Chem. Res.* **2011**, *44*, 424; c) V. W.-W. Yam, K. M.-C. Wong, *Chem. Commun.* **2011**, *47*, 11579.
- [7] a) M. D. Allendorf, C. A. Bauer, R. K. Bhakta, R. J. T. Houk, *Chem. Soc. Rev.* **2009**, *38*, 1330; b) Y. Cui, Y. Yue, G. Qian, B. Chen, *Chem. Rev.* **2012**, *112*, 1126.
- [8] a) E. C. Glazer, D. Magde, Y. Tor, *J. Am. Chem. Soc.* **2005**, *127*, 4190; b) E. C. Glazer, D. Magde, Y. Tor, *J. Am. Chem. Soc.* **2007**, *129*, 8544; c) Y. Leydet, D. M. Bassani, G. Jonusauskas, N. D. McClenaghan, *J. Am. Chem. Soc.* **2007**, *129*, 8688; d) M. Nishikawa, K. Nomoto, S. Kume, K. Inoue, M. Sakai, M. Fujii, H. Nishihara, *J. Am. Chem. Soc.* **2010**, *132*, 9579; e) T. Morimoto, M. Ito, K. Koike, T. Kojima, T. Ozeki, O. Ishitani, *Chem. Eur. J.* **2012**, *18*, 3292; f) Y. Liu, M. Pan, Q.-Y. Yang, L. Fu, K. Li, S.-C. Wei, C.-Y. Su, *Chem. Mater.* **2012**, *24*, 1954; g) X.-c. Shan, F.-l. Jiang, D.-q. Yuan, H.-b. Zhang, M.-y. Wu, L. Chen, J. Wei, S.-q. Zhang, J. Pan, M.-c. Hong, *Chem. Sci.* **2013**, *4*, 1484.
- [9] M. Kasha, *Faraday Soc. Discuss.* **1950**, *9*, 14.
- [10] S.-Z. Zhan, M. Li, X.-P. Zhou, J.-H. Wang, J.-R. Yang, D. Li, *Chem. Commun.* **2011**, *47*, 12441.
- [11] R. Peng, M. Li, D. Li, *Coord. Chem. Rev.* **2010**, *254*, 1, and references therein.
- [12] a) P. D. Harvey, M. Knorr, *Macromol. Rapid Commun.* **2010**, *31*, 808; b) T. H. Kim, Y. W. Shin, J. H. Jung, J. S. Kim, J. Kim, *Angew. Chem.* **2008**, *120*, 697; *Angew. Chem. Int. Ed.* **2008**, *47*, 685; c) J. Y. Lee, S. Y. Lee, W. Sim, K. Park, J. Kim, S. S. Lee, *J. Am. Chem. Soc.* **2008**, *130*, 6902; d) D. Braga, L. Maini, P. P. Mazzeo, B. Ventura, *Chem. Eur. J.* **2010**, *16*, 1553; e) D. Prochowicz, I. Justyniak, A. Kornowicz, T. Kaczorowski, Z. Kaszkur, J. Lewiński, *Chem. Eur. J.* **2012**, *18*, 7367; f) Y. Kang, F. Wang, J. Zhang, X. Bu, *J. Am. Chem. Soc.* **2012**, *134*, 17881; g) J. Y. Lee, H. J. Kim, J. H. Jung, W. Sim, S. S. Lee, *J. Am. Chem. Soc.* **2008**, *130*, 13838.
- [13] a) P. C. Ford, E. Cariati, J. Bourassa, *Chem. Rev.* **1999**, *99*, 3625; b) F. De Angelis, S. Fantacci, A. Sgamellotti, E. Cariati, R. Ugo, P. C. Ford, *Inorg. Chem.* **2006**, *45*, 10576; c) H. Kitagawa, Y. Ozawa, K. Toriumi, *Chem. Commun.* **2010**, *46*, 6302; d) S. Perruchas, X. F. Le Goff, S. Maron, I. Maurin, F. Guillen, A. Garcia, T. Gacoin, J.-P. Boilot, *J. Am. Chem. Soc.* **2010**, *132*, 10967; e) S. Perruchas, C. Tard, X. F. Le Goff, A. Fargues, A. Garcia, S. Kahlal, J.-Y. Saillard, T. Gacoin, J.-P. Boilot, *Inorg. Chem.* **2011**, *50*, 10682; f) Z. Liu, P. I. Djurovich, M. T. Whited, M. E. Thompson, *Inorg. Chem.* **2012**, *51*, 230.
- [14] a) I. I. Vorontsov, A. Y. Kovalevsky, Y.-S. Chen, T. Graber, M. Gembicky, I. V. Novozhilova, M. A. Omary, P. Coppens, *Phys. Rev. Lett.* **2005**, *94*, 193003; b) T. Grimes, M. A. Omary, H. V. R. Dias, T. R. Cundari, *J. Phys. Chem. A* **2006**, *110*, 5823; c) B. Hu, G. Gahungu, J. Zhang, *J. Phys. Chem. A* **2007**, *111*, 4965.
- [15] a) A. A. Mohamed, *Coord. Chem. Rev.* **2010**, *254*, 1918; b) H. V. R. Dias, H. V. K. Diyabalanage, M. A. Rawashdeh-Omary, M. A. Franzman, M. A. Omary, *J. Am. Chem. Soc.* **2003**, *125*, 12072; c) H. V. R. Dias, H. V. K. Diyabalanage, M. G. Eldabaja, O. Elbjerrami, M. A. Rawashdeh-Omary, M. A. Omary, *J. Am. Chem. Soc.* **2005**, *127*, 7489; d) T. Jozak, Y. Sun, Y. Schmitt, S. Lebedkin, M. Kappes, M. Gerhards, W. R. Thiel, *Chem. Eur. J.* **2011**, *17*, 3384; e) G.-F. Gao, M. Li, S.-Z. Zhan, Z. Lv, G.-h. Chen, D. Li, *Chem. Eur. J.* **2011**, *17*, 4113.
- [16] a) J.-P. Zhang, Y.-B. Zhang, J.-B. Lin, X.-M. Chen, *Chem. Rev.* **2012**, *112*, 1001; b) J. He, Y.-G. Yin, T. Wu, D. Li, X.-C. Huang, *Chem. Commun.* **2006**, 2845; c) J.-X. Zhang, J. He, Y.-G. Yin, M.-H. Hu, D. Li, X.-C. Huang, *Inorg. Chem.* **2008**, *47*, 3471; d) J.-P. Zhang, S. Kitagawa, *J. Am. Chem. Soc.* **2008**, *130*, 907; e) L. Hou, W.-J. Shi, Y.-Y. Wang, H.-H. Wang, L. Cui, P.-X. Chen, Q.-Z. Shi, *Inorg. Chem.* **2011**, *50*, 261; f) S.-Z. Zhan, M. Li, X.-P. Zhou, D. Li, S. W. Ng, *RSC Adv.* **2011**, *1*, 1457.
- [17] a) S.-Z. Zhan, D. Li, X.-P. Zhou, X.-H. Zhou, *Inorg. Chem.* **2006**, *45*, 9163; b) S.-Z. Zhan, M. Li, J.-Z. Hou, J. Ni, D. Li, X.-C. Huang, *Chem. Eur. J.* **2008**, *14*, 8916; c) S.-Z. Zhan, R. Peng, S.-H. Lin, S. W. Ng, D. Li, *CrystEngComm* **2010**, *12*, 1385; d) S.-Z. Zhan, M. Li, X.-P. Zhou, J. Ni, X.-C. Huang, D. Li, *Inorg. Chem.* **2011**, *50*, 8879.
- [18] G. M. Sheldrick, *Acta Crystallogr.* **2008**, *A64*, 112.
- [19] O. V. Dolomanov, A. J. Blake, N. R. Champness, M. Schröder, *J. Appl. Crystallogr.* **2003**, *36*, 1283.

- [20] A. L. Spek, *J. Appl. Crystallogr.* **2003**, *36*, 7.
- [21] a) M. A. Omary, M. A. Rawashdeh-Omary, M. W. A. Gonser, O. Elbjeirami, T. Grimes, T. R. Cundari, *Inorg. Chem.* **2005**, *44*, 8200; b) F. Gong, Q. Wang, J. Chen, Z. Yang, M. Liu, S. Li, G. Yang, *Inorg. Chem.* **2010**, *49*, 1658.
- [22] a) H. V. R. Dias, C. S. P. Gamage, *Angew. Chem.* **2007**, *119*, 2242; *Angew. Chem. Int. Ed.* **2007**, *46*, 2192; b) S. M. Tekarli, T. R. Cundari, M. A. Omary, *J. Am. Chem. Soc.* **2008**, *130*, 1669; c) M. A. Rawashdeh-Omary, M. D. Rashdan, S. Dharanipathi, O. Elbjeirami, P. Ramesh, H. V. R. Dias, *Chem. Commun.* **2011**, *47*, 1160; d) C. Yang, O. Elbjeirami, C. S. P. Gamage, H. V. R. Dias, M. A. Omary, *Chem. Commun.* **2011**, *47*, 7434.
- [23] a) S. E. Braslavsky, *Pure Appl. Chem.* **2007**, *79*, 293, web link: <http://goldbook.iupac.org/I03310.html>; b) J. K. Nagle, B. A. Brennan, *J. Am. Chem. Soc.* **1988**, *110*, 5932; c) S. A. Clodfelter, T. M. Doede, B. A. Brennan, J. K. Nagle, D. P. Bender, W. A. Turner, P. M. LaPunzina, *J. Am. Chem. Soc.* **1994**, *116*, 11379.
- [24] The coined chemopalette concept can also be generalized to embrace broader supramolecular territories that involve nano- and bio-functionalities. See, for example: G. Liu, D.-Q. Feng, W.-J. Zheng, T. Chen, L. Qi, D. Li, *J. Mater. Chem. B* **2013**, *1*, 2128.

Received: December 30, 2012

Revised: April 30, 2013

Published online: June 18, 2013